Propagating Schallamach-type waves resemble interface cracks

Mohammad Aaquib Ansari and Koushik Viswanathan*
Department of Mechanical Engineering, Indian Institute of Science, Bangalore 560012, India

(Received 1 April 2021; revised 19 January 2022; accepted 1 March 2022; published 18 April 2022)

Intermittent motion, called stick-slip, is a friction instability that commonly occurs during relative sliding of two elastic solids. In adhesive polymer contacts, where elasticity and interface adhesion are strongly coupled, stick-slip arises due to the propagation of slow detachment waves at the interface. Here we analyze two distinct detachment waves moving parallel (Schallamach wave) and antiparallel (separation wave) to applied remote sliding. Both waves cause slip in the same direction, travel at speeds much lesser than any elastic wave speed, and are therefore describable using the same perturbative elastodynamic framework with identical boundary conditions. A numerical scheme is used to obtain interface stresses and velocities for arbitrary Poisson ratio, along with closed-form solutions for incompressible solids. Our calculations reveal a close correspondence between moving detachment waves and bimaterial interface cracks, including the nature of the singularity and the functional forms of the stresses. Based on this correspondence, and coupled with a fracture analogy for dynamic friction, we develop a phase diagram showing domains of possible occurrence of stick-slip via detachment waves vis-á-vis steady interface sliding. Our results have interesting implications for sliding and stick-slip phenomena at soft interfaces.

DOI: 10.1103/PhysRevE.105.045002

I. INTRODUCTION

Consider a simple system consisting of two rectangular solid blocks, one elastic and the other relatively rigid, that are pressed into contact and slid remotely at constant velocity V_0. Elementary considerations dictate that the interface will start sliding once the shear force exceeds the static friction threshold, commonly assumed to depend on the friction coefficient μ_s and the normal force F_N. That this rudimentary picture is simply not universally true is borne out dramatically by earthquake faults, squealing brakes and violin strings [1–4]. These systems exhibit what is known as stick-slip, a phenomenon wherein the interface moves only intermittently even though the contacting solids are slid remotely at constant speed.

Several plausible explanations for stick-slip have now been established, hinging primarily on velocity dependence of the interface friction force [2,5–7] and/or some type of regularization [8,9]. Most commonly studied models for understanding the repeated static-dynamic-static transitions occurring during stick-slip are of the Burridge-Knopoff type [10–12]. These models, originally applied to earthquake fault motion, are characterized by a chain of horizontal and vertical springs connecting both sliding bodies at the interface, coupled with a suitable interface friction law. In the continuum limit of these models, slip mediating interface fronts propagate at or close to the speed of sound in the material [13]. On the continuum scale, such fast moving waves are describable within linear elastodynamics, even though the exact propagation velocity is determined by the particular boundary conditions involved [14–16]. Nonetheless, these fronts almost always propagate at speeds comparable to the Rayleigh wave speed [17–19], which is a material property. A notable exception is the recent work of Trømborg *et al.* [20] which describes a multi-scale model for slow fronts, albeit by exploiting a suitably defined velocity scale.

On the contrary, soft material contacts can exhibit stick-slip via more subtle mechanisms [21]. This complication is primarily because the effects of friction, adhesion and elastic deformation cannot be decoupled. Under many conditions, soft adhesive interfaces can slip only via the propagation of slow moving pulselike fronts, with unique dynamics, often involving simultaneous interface detachment and reattachment [22,23]. A well-known example of such a detachment wave is the Schallamach wave in rubbers [24], which results from local interface buckling [25–30]. Detachment waves of this nature are often described by analogy with the motion of a ruck in a carpet [31,32]: If a carpet is to be moved by distance Δx, then we could either simply translate the entire carpet surface at once by Δx or create a localized slip zone by buckling—causing slip Δx—that then propagates along the carpet and progressively causes it to slip. This buckling and detachment type mechanism is quite general and also occurs during motion of soft-bodied insects such as caterpillars and earthworms [33,34].

Interface detachment waves of this nature are typically characterized by their dramatically low propagation velocity, compared to typical elastic wave speeds [35]; a fact that makes them difficult to describe theoretically. Consequently, several questions about the propagation of slow detachment waves at soft interfaces remain unanswered and are the subject of the present manuscript. Motivated by a recently described correspondence between friction and fracture [36,37], we attempt to establish a relationship between detachment wave motion

*koushik@iisc.ac.in

and crack growth in soft interfaces. Such a relationship can then be used to predict when detachment waves, and consequently stick-slip, will occur at the expense of steady uniform sliding.

The manuscript is organized as follows. We first present experimental observations of detachment waves at a typical soft adhesive elastic interface that build on our recent results showing the occurrence of opposite moving detachment waves (Sec. II). The data presented herein is new and complements our earlier observations. In Sec. III, we present a common theoretical treatment of these waves using a linear elastodynamic model. We obtain analytical solutions for incompressible solids and numerically evaluate interface stresses and velocities for arbitrary Poisson ratio. Based on this treatment, a fundamental analogy with interface fracture is established. We study the nature of the singularity ahead of the leading edge of a slow moving detachment wave and show that it resembles a statically loaded interface crack. Our results allow us to construct a hypothetical " phase diagram" for the occurrence of slow frictional waves at soft interfaces. We discuss the implications of our results in Sec. IV and present some concluding remarks in Sec. V.

II. BACKGROUND: EXPERIMENTAL OBSERVATIONS OF SLOW DETACHMENT WAVES

Before we embark on a theoretical analysis of slow moving detachment waves at adhesive interfaces, we first present experimental data outlining their primary properties. While most experimental studies of sliding friction use a spherical indenter geometry, detachment waves are best observed using a cylindrical geometry. This is because the latter can help isolate single wave events without any intervening edge effects. The configuration is shown in Fig. 1 and is the same as that used by one of the present authors in prior studies [38]. For additional details, such as sample or indenter dimensions and material elastic properties, the reader is referred to this article. We provide only the essential data here to retain continuity with the rest of the manuscript.

The schematic in Fig. 1(a) shows a model adhesive contact interface between an elastic polymer (PDMS, Dow Corning Sylgard 184) and a rigid cylindrical lens (Edmund Optics). The geometry of the contact interface (xy plane) is such that it resembles an "adhesive channel" so that single waves may be easily isolated. The lens and polymer were brought into contact by a normal load $F_N \sim 50$ mN, adjusted so that the initial contact width was constant $= 1$ mm in the y direction. The long aspect ratio of the contact also implied that the lens and polymer had to be aligned with care to maintain constant contact width. The contact region was illuminated using a backlight source and imaged using a high-speed camera. Simultaneously, normal and shear forces were measured using a piezoelectric dynamometer (Kistler). A sample image of the contact region is shown in Fig. 1(b). Prior to any experiment, contact was first established and maintained for a fixed time $t = 60$ s to standardize any possible contact aging effects. The polymer was then slid relative to the lens using a linear stage at constant speeds $V_0 = 10$ μm/s to 20 mm/s, for a distance of 30 mm (sample length was 70 mm).

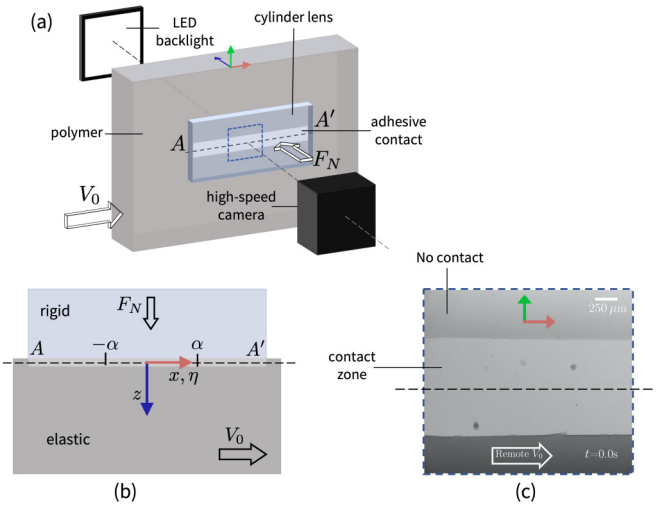

FIG. 1. Experimental setup and coordinate conventions used in the text. (a) Schematic showing polymer-lens contact geometry and sliding conditions. The xyz axes are also shown as red, green and blue arrows, respectively. Note that the origin of coordinates is at the center of the contact and not at the top face as indicated here for convenience. (b) Approximate 2D side view of the interface; the comoving angular coordinate η coincides with the physical x (see text) and (c) sample camera image showing adhesive contact zone (light gray) distinguished from the rest of the polymer (dark gray). Remotely applied V_0 is always taken to be from left to right, along the x axis.

The *in situ* images revealed the interface dynamics accompanying interface stick-slip under steady remote sliding. At low V_0, the interface shows rich spatiotemporal dynamics—remaining stationary for long periods, separated by periods of localized slip. These slip events are solely mediated by the propagation of two distinct detachment waves, moving parallel (Schallamach wave) and antiparallel (separation pulse) to V_0, henceforth denoted $+$ and $-$ waves. While the former is well known [24], its less illustrious sibling was first reported in Ref. [38]. Sample image sequences showing their propagation properties are shown in Fig. 2, with the remote sliding direction V_0 also marked. Corresponding movies are presented as supplementary material [39].

The three frames in the top panel depict a single moving Schallamach or $+$ wave within the interface, $V_0 = 0.5$ mm/s. It moves in the same direction as V_0 and shows several typical features. First, the detachment zone (dark) has a characteristic V shape with wrinkles on its surface. The wrinkles form locally as the wave progresses and result in imperfect contact in its wake. Second, points on the interface remain stationary before and after wave passage; they only translate in the V_0 direction when the wave propagates past them. This is clearly shown by the motion of a marker particle that is located just below the PDMS surface (black in figure). The marker is translated by the $+$ wave so that it slips a finite distance Δx_+ after the wave has passed. Note that the amount of slip Δx is nearly equal to the extent of the wave in the propagation direction. Third, the timestamps show that the wave propagates at a constant speed $c_+ \gg V_0$. It is further clear that c_+ ($\sim$0.1 m/s) is much lower than any elastic wave speed in the

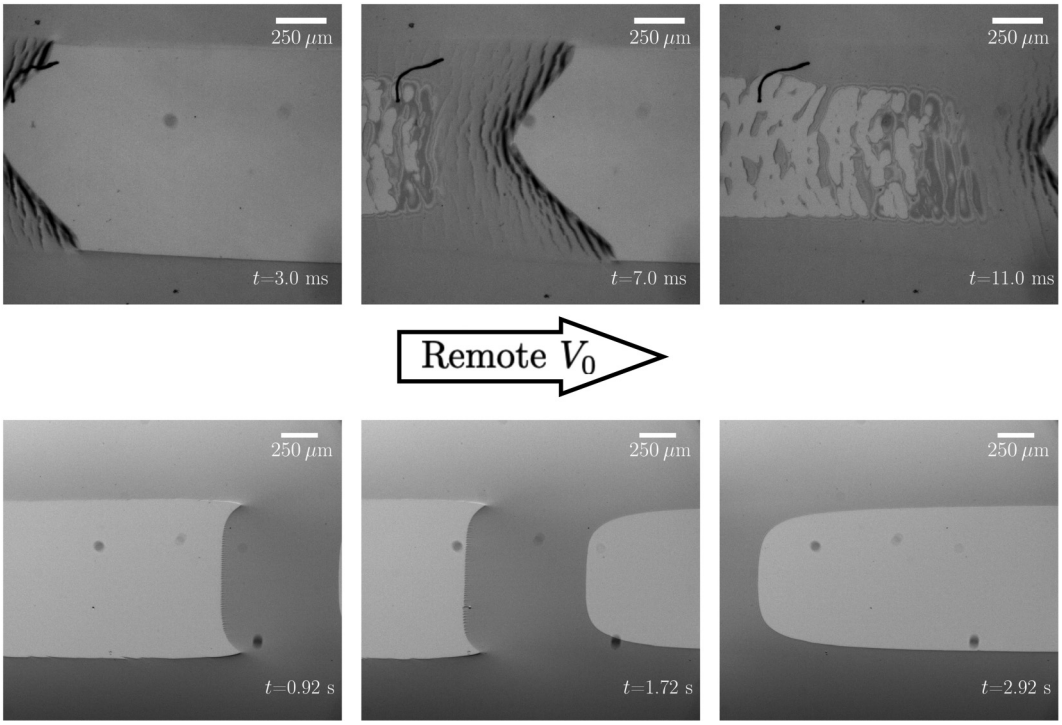

FIG. 2. High-speed *in situ* images showing two distinct detachment waves at the polymer-lens interface. Top row shows a Schallamach (+) wave propagating in the same direction as remotely applied V_0. Note the timescale for wave propagation is significantly lesser than that for uniform sliding. Bottom row shows a separation (−) wave propagating in the opposite direction. Applied velocity $V_0 = 0.5$ mm/s (top row) and 0.05 mm/s (bottom row).

material, cf. Rayleigh wave speed $c_R \sim 10$–100 m/s. Finally, once the wave has passed, the entire sequence repeats with another wave. Such single wave events occur at a constant frequency n_+ such that $n_+ \Delta x_+ = V_0$, as established in prior work [30].

The lower panel in Fig. 2 shows a very different type of wave—the separation (−) wave—that propagates in the opposite direction to V_0 while causing slip in the same direction. In this sense, this wave may be thought of as the dual of the Schallamach wave. It shares some similarities with the + or Schallamach wave described above, viz. causing constant interface slip Δx_- comparable to its width, and slow velocity of propagation c_- that obeys $V_0 < c_- \ll c_R$ as before. Yet, this − wave is fundamentally different in that it propagates in the direction opposite to V_0, despite surface slip being in the same direction as V_0. The detachment zone has a shape quite different from the V shape of the + wave and is also devoid of any compression-induced wrinkles, so that complete readhesion occurs in its wake. Once a single wave propagates, the entire process repeats and interface motion occurs in steps, similar to + waves. While V_0 is different for the two cases presented, it is generally observed that $c_+/V_0 \sim 50$–100 and $c_-/V_0 \sim 10$–50. Furthermore, $c_- < c_+$ and the frequency $n_- < n_+$, as reported in our earlier work [38].

At the macroscale, the effect of intermittent interface motion due to repeated wave propagation events is recorded by measuring the shear force as a function of time, see Fig. 3. The corresponding nondimensional force traces for + and − waves are shown in the left and right panels of this figure, respectively. The shear force is normalized by the product GA of the shear modulus G and the nominal contact area A. Time is nondimensionalized by the time taken (t_0) for the entire length (L) of the interface to slip uniformly at speed V_0. The V_0 values for the + and − waves corresponding to the data in this figure are 0.5 mm/s and 0.05 mm/s, respectively.

Repeated wave motion results in oscillatory shear forces—a characteristic of stick-slip motion—with distinct frequency and amplitude reduction. For the case of + waves, Fig. 3 (left), the force initially builds up as the interface is stationary and the shear stress on the interface increases. This built up stress is then released by the propagation of a single + wave and a corresponding force reduction is observed in the figure. Each subsequent cycle corresponds to the propagation of one such wave at the interface. The timescale for wave propagation is also much smaller than that for remote sliding $t_0 = L/V_0$. In

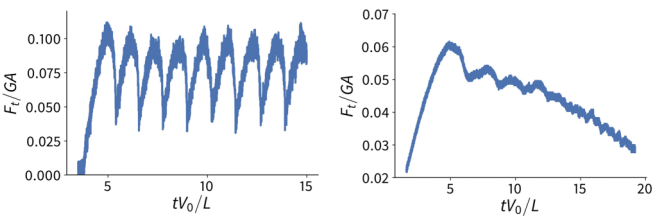

FIG. 3. Shear force measured simultaneous with multiple wave propagation events for Schallamach (+) waves (left) and separation pulse (− wave, right). The horizontal axis is nondimensionalized by time $t_0 = L/V_0$. Applied velocity $V_0 = 0.5$ mm/s (left) and 0.05 mm/s (right).

comparison with + waves, the propagation of − waves is accompanied by a smaller force reduction and a lower frequency n_-. Furthermore, the force trace eventually decays to zero after the first few wave events, likely due to viscoelastic relaxation and minor misalignment between the PDMS and indenter. A similar decay is also seen in the case of + waves but does not appear in Fig. 3 (left) due to the higher V_0 and, consequently, lower t_0 in this plot.

In summary, interface motion is not continuous but occurs intermittently via single slip events. While we have focused exclusively on wave propagation here, nucleation events leading to single waves have been addressed in our prior work [30,38]. It has been shown that the magnitude of V_0 determines which wave will nucleate at the edge of the contact. However, post-nucleation, slip events are solely mediated either by Schallamach (+) or separation (−) waves propagating parallel or antiparallel to V_0, respectively. Both waves propagate at speeds $c_\pm$ that are much slower than any characteristic elastic wave speed in the material. They also retain their shape within the interface and result in constant finite slip $\Delta x_\pm$ in the same direction as V_0. The net macroscale effect of this periodic wave propagation is stick-slip motion of the interface.

III. THEORETICAL ANALYSIS OF SLOW MOVING DETACHMENT WAVES

It is clear from the experimental background presented in Sec. II that propagating ± waves show unique properties, viz. slow propagation velocity and effecting interface slip, that are not characteristic of elastic surface waves in general [14]. We now attempt to explain these features using a theoretical elastodynamic framework. A quasi-three-dimensional (3D) version of this framework was introduced in our prior work [40]. In this section, we present a fully 2D model, obtain solutions for both compressible and incompressible materials, and explore their consequences.

A. Geometry and framework

We assume that the elastic polymer and the rigid indenter occupy the $z \geqslant 0$ and $z < 0$ half-spaces, respectively, see Fig. 1(b), and that V_0 is applied along the x direction at $z \to -\infty$. Detachment waves propagate along the $\pm x$ directions on the $z = 0$ interface, with signed wave speed c; the domain length along this axis is L. In order to eliminate uncertainties induced by wave nucleation, we use periodic boundary conditions at $x = \pm L/2$. This is justified by the constant wave speed c and the fact that that only a single wave is present within the domain $x \in (-L/2, L/2)$ at any instant (cf. Fig. 2). We use a comoving reference frame with angular coordinate $\eta = k(x - ct)$ in which the wave is stationary. Here k denotes the wave number and is related to physical parameters in the problem, as discussed in Appendix. This type of periodic comoving construction [Fig. 1(b)] is commonly used for describing wave propagation phenomena, see, e.g., Refs. [15,16,41] and the discussion in Ref. [42].

Within this system, the interface is separated into two zones—a sticking zone ($\alpha < |\eta| < \pi$) with zero velocity, and a slipping detached zone ($|\eta| < \alpha$), comprising the wave itself, with zero stress. Note that the angular wave extent 2α, when expressed in physical units, is nearly equal to the amount of slip Δx (cf. Fig. 2). The corresponding boundary conditions are spelt out in Appendix. First, we define nondimensional versions $\Psi(s)$, $\Phi(s)$ of the interface velocities $\dot{u}_x$, $\dot{u}_z$ as:

$$\Psi(s) = \frac{\dot{u}_x(s)}{c(1 + a^2 s^2)} \qquad \Phi(s) = \frac{\dot{u}_z(s)}{c(1 + a^2 s^2)}, \tag{1}$$

where $\dot{u}_x$ and $\dot{u}_z$ are horizontal and vertical interface ($z = 0$) velocities, $a = \tan\frac{\alpha}{2}$ and $s = \frac{1}{a}\tan\frac{\eta}{2}$ are dimensionless variables representing the detachment zone width and spatial location, respectively, and c is the wave speed defined earlier. Note that the wave extent corresponds to $|s| < 1$. Using the procedure described in the Appendix, it can be shown that $\Phi(s)$ and $\Psi(s)$ are governed by coupled singular integral equations ($|s|, |p| < 1$):

$$\begin{aligned}
&\frac{\tau_r}{G} + \frac{2k_1}{\pi}\left[(1 + a^2p^2)\int_{-1}^{1}\frac{\Psi(s)ds}{s - p} + \pi a\frac{V_0}{c}p\right] \\
&\quad - 2k_2(1 + a^2p^2)\Phi(p) = 0 \\
&\frac{\sigma_r}{G} - 2k_2\frac{V_0}{c} + \frac{2k_1}{\pi}(1 + a^2p^2)\int_{-1}^{1}\frac{\Phi(s)ds}{s - p} \\
&\quad + 2k_2(1 + a^2p^2)\Psi(p) = 0.
\end{aligned} \tag{2}$$

Here G and ν are the shear modulus and Poisson ratio, respectively, and the dimensionless constants $k_1 = \frac{2(1-\nu)}{3-4\nu}$ and $k_2 = \frac{1-2\nu}{3-4\nu}$. The remote ($z \to -\infty$) normal and shear stresses are denoted σ_r and τ_r, respectively [see Appendix, especially the discussion following Eq. (A1)].

Singular integral equations (SIEs) of this form are commonly supplemented by side conditions [43]. In the present case, these side conditions are given by

$$\int_{-1}^{1}\Psi(s)ds = \frac{\pi V_0}{ac} \qquad \int_{-1}^{1}\Phi(s)ds = 0. \tag{3}$$

The rest of this section pertains to elucidating the physical implications of Eq. (2) under various conditions.

B. Exact solution for $\nu = 0.5$: Existence of + and − waves

When the elastic polymer is incompressible ($\nu = 0.5$), the constants $k_1 = 1$ and $k_2 = 0$ in Eq. (2), so that the two SIEs are decoupled. Physically, this means that the normal and tangential direction elastic fields are independent of each other. The corresponding interface velocities are found by direct inversion [43]

$$\begin{aligned}
\Phi(p) &= -\frac{\sigma_r}{2G}\frac{p}{\sqrt{1 - p^2}}\frac{\sqrt{1 + a^2}}{1 + a^2p^2} \\
\Psi(p) &= \frac{1}{\sqrt{1 - p^2}}\left[\left(\frac{V_0}{c\,a}\right)\frac{\sqrt{1 + a^2}}{1 + a^2p^2} - \frac{\tau_r}{2G}\frac{p\sqrt{1 + a^2}}{1 + a^2p^2}\right],
\end{aligned} \tag{4}$$

from which the final dimensional forms of $\dot{u}_x(x, t)$ and $\dot{u}_z(x, t)$ are easily obtained using Eq. (1).

Note that Eq. (2) is obtained from the boundary condition that the detachment zone is traction free. Consequently, outside the detachment and within the stick zone $|s|, |p| > 1$, the right-hand side of this equation is nonzero and gives the

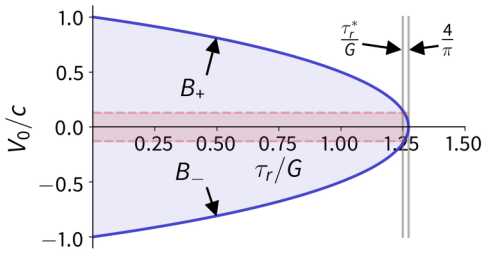

FIG. 4. Diagram showing existence of two branches $B_\pm$ corresponding to $\pm$ detachment waves. Any c between the two bounding curves (solid blue) is permitted for wave propagation. The value τ_r^*/G represents the formal limit beyond which wave propagation ceases, while the two branches $B_\pm$ meet at $\tau_r/G = 4/\pi$. Both these values are shown as vertical gray lines. The region bounded by the horizontal dashed red lines represents breakdown of the proposed perturbative analysis.

corresponding stresses $\sigma(p)$ and $\tau(p)$. Here the left-hand side of the equation is no longer a singular integral and readily yields:

$$\frac{\sigma}{\sigma_r} = \frac{|p|\sqrt{1+a^2}}{\sqrt{p^2-1}}$$
$$\frac{\tau}{\tau_r} = \frac{|p|\sqrt{1+a^2}}{\sqrt{p^2-1}} - \left(\frac{V_0}{ac}\right)\left(\frac{2G}{\tau_r}\right)\frac{\sqrt{1+a^2}}{\sqrt{p^2-1}}\frac{|p|}{p}. \tag{5}$$

Enforcing the physical constraint that $\dot{u}_x(\eta)$ is everywhere in the same direction as V_0 [see Appendix, Eq. (A2)] in Eq. (4) results in the condition

$$\left[\frac{\tan(\pi V_0/2c)}{\pi V_0/2c}\right] \geqslant \frac{4G}{\pi\tau_r}. \tag{6}$$

This inequality, involving V_0, c, and τ_r, puts a constraint on the existence of physically relevant wave solutions to the governing SIEs. Consequently, we may plot an existence diagram showing two branches B_+, B_- that satisfy Eq. (6), see Fig. 4. These branches correspond to $c/V_0 > 0$ (+ wave branch) $c/V_0 < 0$ (− wave branch), respectively. The minimum allowable wave speed c_+ or c_- for a given value of τ_R is determined by the curve $B_\pm$; all wave velocities c lying between $B_\pm$ (shaded region in Fig. 4) are therefore permissible. Thus, the wave speed is not fixed *a priori* by a material velocity scale but is instead determined by the interface conditions post wave nucleation. Additionally, the + wave and − wave branches obtained from Eq. (6) are perfectly symmetric. While this symmetry is restricted to the propagation velocity alone, it does not predict the speed at which $\pm$ waves actually propagate. This latter feature is solely determined by the nucleation mechanics; we discuss this proposition in Sec. IV.

It is also clear from Fig. 4 that $B_\pm$ merge at $\tau_r/G = 4/\pi$. At this point, the envelope of allowed wave speeds shrinks to zero and for $\tau_r/G > 4/\pi$, physically relevant propagating wave solutions are not possible. However, this exact limit is not reached in practice since a narrow region close to the horizontal axis (bound by dashed red lines in the figure) must be excluded from consideration. Within this region, $c_\pm$ is no longer small compared to c_L and c_T so that the entire perturbative formulation is invalid. The corresponding maximum τ_r value is generically denoted τ_r^*, see vertical dashed line in Fig. 4. For fixed $V_0 \sim 10^{-2}$ m/s as used in the experiments of Sec. II, τ_r is not appreciably different from G. This region must nonethess be excluded from our further discussion. The bifurcation diagram in Fig. 4 hence shows the domain of existence of opposite moving slow $\pm$ detachment waves within the elastic framework.

The interface displacements are obtained for both $\pm$ waves [shaded region between solid blue and dashed red lines in Fig. 4] by integrating the velocities in Eq. (4). The vertical displacement in the detachment zone is determined from $\dot{u}_z$

$$\frac{u_z}{\Delta x} = -\left(\frac{c}{2\pi V_0}\right)\left(\frac{\sigma_r}{G}\right)\tanh^{-1}\left(\frac{a\sqrt{1-p^2}}{\sqrt{1+a^2}}\right). \tag{7}$$

Note that the constant of integration is fixed by the condition that the interface readheres after wave passage and no net z displacement is induced for both $\pm$ waves, cf. Fig. 2.

The x displacement is also obtained similarly, but the constant of integration must now be set a little more carefully, depending on which branch in Fig. 4 we are describing. This is because the location of points before and after wave passage depends on the sign of c/V_0, see Appendix, Eq. (A2). Hence, the condition on u_x in Eq. (A2) must be enforced separately for the + and − branches.

For a Schallamach (+) wave, we obtain

$$\frac{u_x}{\Delta x} = -\frac{1}{\pi}\left[\tan^{-1}\left(\frac{p\sqrt{1+a^2}}{\sqrt{1-p^2}}\right) + \frac{c\tau_r}{2GV_0}\tanh^{-1}\left(\frac{a\sqrt{1-p^2}}{\sqrt{1+a^2}}\right)\right] + \frac{1}{2}, \tag{8}$$

while for the separation (−) wave,

$$\frac{u_x}{\Delta x} = \frac{1}{\pi}\left[\tan^{-1}\left(\frac{p\sqrt{1+a^2}}{\sqrt{1-p^2}}\right) - \frac{c\tau_r}{2GV_0}\tanh^{-1}\left(\frac{a\sqrt{1-p^2}}{\sqrt{1+a^2}}\right)\right] + \frac{1}{2}. \tag{9}$$

These relations fully resolve the interface dynamics for $\nu = 0.5$. Features of the solutions in Eqs. (4), (5), (8), and (9) are presented in the next section after discussing the solution of the fully coupled ($\nu \neq 0.5$) problem.

C. Numerical solution for $\nu \neq 0.5$

For general elastic media with arbitrary ν, the original SIE system in Eq. (2) can be cast in the form of a matrix equation:

$$\begin{bmatrix} -m & 0 \\ 0 & m \end{bmatrix}\begin{bmatrix}\Phi(p)\\ \Psi(p)\end{bmatrix} + \frac{1}{\pi}\begin{bmatrix}0 & 1\\ 1 & 0\end{bmatrix}\int_{-1}^{1}\begin{bmatrix}\Phi(u)\\ \Psi(u)\end{bmatrix}\frac{du}{u-p} = \begin{bmatrix} -\frac{\tau_r}{2k_1G(1+a^2p^2)} - 2aV_0/c \\ \frac{2k_2V_0/c - \sigma_r/G}{2k_1(1+a^2p^2)}\end{bmatrix}, \tag{10}$$

where $m = k_2/k_1$ and with the additional conditions of Eq. (3) as before.

In order to solve this coupled system numerically, we invert the SIEs using special function approximations [44]. First, we introduce the complex variable $\chi = \Phi + i\Psi$ so that

Eq. (10) is

$$-m\chi - \frac{i}{\pi}\int_{-1}^{1}\frac{\chi(u)du}{u-p} = g_1 - ig_2 = g(\chi), \tag{11}$$

where the right-hand side of Eq. (10) is represented as $(g_1 \quad g_2)^T$ without loss of any generality. Just as with the $\nu = 0.5$ case, we expect the solution to be singular at both ends $p = \pm 1$, so that this complex valued SIE can be solved numerically using Jacobi polynomials $P_n^{(\xi,\zeta)}(p)$. To find the solution of Eq. (11), we consequently have to determine coefficients c_n such that

$$\chi(p) = \sum_0^\infty c_n w(p) P_n^{(\xi,\zeta)}(p), \tag{12}$$

where the weight functions $w(p)$ for Jacobi polynomials (unbounded at both $p = \pm 1$) are given by

$$w(p) = (1-p)^\xi (1+p)^\zeta \quad \xi = -\frac{1}{2} - i\omega \quad \zeta = -\frac{1}{2} + i\omega$$
$$\omega = \frac{1}{2\pi}\log\left(\frac{1+m}{1-m}\right) \tag{13}$$

with $m = \frac{1-2\nu}{2(1-\nu)} = k_2/k_1$, as defined in Eq. (11).

The side condition in Eq. (3) is now $\int_{-1}^{1}\chi(t)dt = \frac{i\pi V_0}{ac}$. An approximate solution for χ is readily obtained if the infinite series in Eq. (12) is terminated with a finite number of terms. Using orthogonality of Jacobi polynomials, the coefficients obey [45]

$$\frac{i}{2\sin\pi\xi}\theta_k(-\xi,-\zeta)c_{1+k} = F_k \tag{14}$$

for $k = 0, 1, 2, \ldots$ where

$$F_k = \int_{-1}^{1} P_k^{(-\xi,-\zeta)}(x)\frac{g(x)dx}{w(x)}, \tag{15}$$

$$\theta_k(\xi,\zeta) = \frac{2^{\xi+\zeta+1}}{2k+\xi+\zeta+1}\frac{\Gamma(k+\xi+1)\Gamma(k+\zeta+1)}{k!\Gamma(k+\xi+\zeta+1)}, \tag{16}$$

$$\theta_0(\xi,\zeta) = \frac{i\pi V_0}{ac} = \frac{2^{\xi+\zeta+1}\Gamma(\xi+1)\Gamma(\zeta+1)}{\Gamma(\xi+\zeta+2)}. \tag{17}$$

We can now solve for $c_1, c_2, \ldots$, using Eq. (14) and the corresponding expressions for θ_k and F_k.

The result of this numerical procedure is an n-term expansion for the interface velocities $\dot{u}_z, \dot{u}_x$ in terms of Jacobi polynomials. It was found that when the detachment zone is small ($a \ll 1$), only two terms in the expansion are sufficient. This was verified in two ways—first by solving the $\nu = 0.5$ case numerically and comparing with the exact result presented in Sec. III B and, second, by explicitly verifying that $|c_n/c_2| \ll 1$ for $n > 2$. The $\nu = 0.5$ solution was reproduced almost exactly by the numerical scheme with $n = 2$.

We now discuss various features of the interface velocities and stresses accompanying wave propagation obtained using this scheme. The existence of two wave solutions even for $\nu \neq 0.5$ may be seen by analytic continuation of the $\nu = 0.5$ solution (Fig. 4) for arbitrary ν. Additionally, the two solutions still remain symmetric as before as explicitly verified by the change $c \to -c$. This is not unexpected since $\nu \neq 0.5$ only couples the normal and shear components but does not in any way change the symmetry in the problem. The results presented next are all for $\alpha = \pi/10$ and $\tau_r/\sigma_r = 5$, unless stated otherwise.

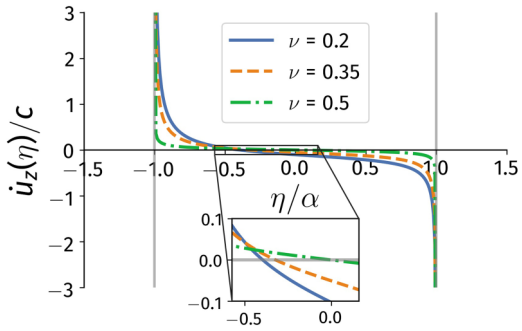

FIG. 5. Interface z velocity showing detaching and reattaching zones within the wave, as a function of ν. Inset shows crossover points for $\dot{u}_z > 0$ and $\dot{u}_z < 0$ for different ν.

The vertical velocity $\dot{u}_z(\eta)$ within the detachment zone is shown in Fig. 5 for $\nu = 0.2, 0.35$ and 0.5. Note that the velocity is zero for $\alpha < |\eta| < \pi$ in accordance with the boundary conditions, see Appendix, Eq. (A1). Several features are immediately noticeable. First, the positive (negative) part of the curve represents interface detachment (reattachment). The velocities are unbounded at the ends $\eta = \pm\alpha$ as expected from both the analytical and numerical solutions. Second, it is clear that the $\nu = 0.5$ curve is perfectly antisymmetric with the interface stationary in the comoving frame exactly at $\eta = 0$ (see inset). This stationary point is the same irrespective of both V_0 and c (+ or − waves), as can be checked from Eq. (4). However, for $\nu = 0.2, 0.35$, the stationary point is away from $\eta = 0$, its precise location being a function of V_0, σ_r, and τ_r. As ν becomes smaller, the point shifts to the left (right) for $c > 0$ (< 0). Finally, all three curves appear very close (but do not meet) near $\eta \simeq -0.4\alpha$. The only significance that may be attached with this point on the physical interface is that its velocity is nearly independent of ν.

The horizontal velocity shows very interesting dynamics, see Fig. 6, for conditions identical to that for Fig. 5. First, the velocity $\dot{u}_x/c$ is always positive, due to the imposed physical

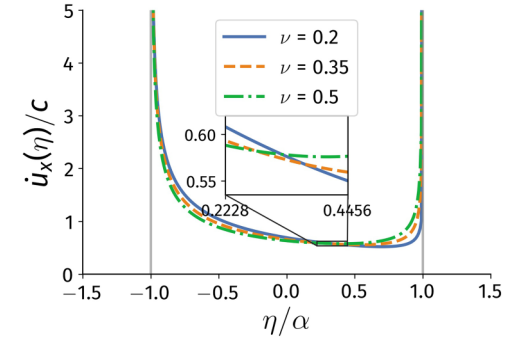

FIG. 6. Interface horizontal velocity $\dot{u}_x(\eta)$ within the detachment zone for various values of ν. Curves for different ν do not meet at a common point.

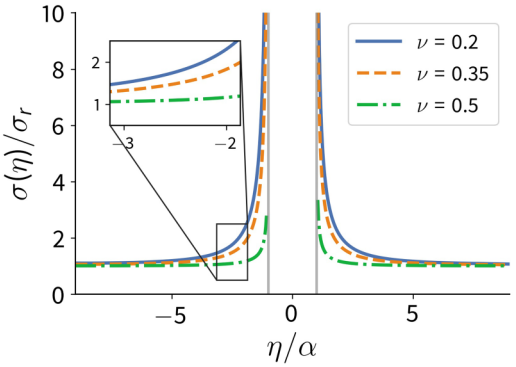

FIG. 7. Normal stress variation along the interface ahead and behind a moving detachment wave. Note that the stresses are constant $\sigma(\eta) = \sigma_r$ far away from the detachment zone and zero within, as per the applied boundary conditions.

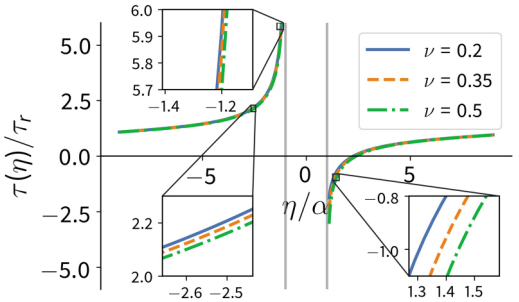

FIG. 8. Tangential stresses accompanying the motion of a single detachment wave. The shear stress singularity changes sign on either side of the wave, corresponding to detachment and reattachment. $\tau/\tau_r \to 1$ as $\eta \to \pm\pi$ and $\tau/\tau_r = 0$ within the detachment zone.

constraints, see Eq. (A2). As with $\dot{u}_z$, it is also unbounded at both ends $\eta = \pm\alpha$ for all ν values. Second, and analogously to the $\dot{u}_z$ case, the interface velocity becomes independent of ν at a fixed location $\eta \simeq +0.3\alpha$. Even though the curves do not meet exactly (see inset), interface locations corresponding to $\eta = +0.3\alpha$ move at the same speed as they would if the material were incompressible. Finally, as ν deviates from 0.5, the $\dot{u}_x$ curve becomes less (more) steep at the trailing (leading) edge $\eta = -\alpha(+\alpha)$. This behavior is due to the enhanced coupling between the horizontal and normal directions at lower values of ν.

We now turn to the interface stresses as the wave propagates. These are complementary to the velocities and are nonzero only outside the contact zone. The normal stress variation for $\nu = 0.2, 0.35, 0.5$ ($\alpha = \pi/10$ is fixed) is shown in Fig. 7. In all three cases, the normal stress is unbounded as $\eta \to \pm\alpha^{\pm}$. Note that here $\pm\alpha^{\pm}$ is here defined as:

$$\alpha^{\pm} = \lim_{\epsilon \to 0^+} \alpha \pm \epsilon. \tag{18}$$

Unboundedness at contact edges is a well-known characteristic of adhesive contacts [46] and shows that the need for adhesion emerges naturally from the solution of the problem, without explicit specification in any of the boundary conditions. Furthermore, the $\nu = 0.5$ curve immediately decays to the remote value σ_r both ahead and behind the detachment zone. This decay is much more gradual for smaller ν so that significant normal stress deviation ($\sigma/\sigma_r \neq 1$) occurs over a larger part of the sticking zone when $\nu = 0.2$. This has important consequences for the occurrence of these waves, as discussed in Sec. III E.

The shear stresses for $\nu = 0.2, 0.35, 0.5$ are unbounded at $\eta \to \pm\alpha^{\pm}$ and appear to be nearly indistinguishable in the linear plot of Fig. 8, in stark contrast to the σ curve, and is due to τ_r being comparatively larger than σ_r ($\tau_r = 5\sigma_r$ by assumption). They indeed differ very little near the $\eta = -\alpha$ edge or even for smaller $\eta < -\alpha$ (see insets). As $\eta \to \pi$, $\tau/\tau_r \to 1$ as is expected. However, the effect of ν is clearer away from the extreme ends of the contact. Here, the three curves are comparatively more distinct (see inset, right) with the $\nu = 0.5$ curve decaying the slowest, in contrast to the normal stress case (Fig. 7). Also noteworthy are the opposite signs of the shear stress at the left and right ends of the detachment zone $\eta = \pm\alpha$. This reflects the need for the interface to reattach under an applied remote shear load, its implications will be explored further in Sec. III F. Finally, given this sign change, there exists a point on the interface where $\tau = 0$, its exact location depends on ν.

D. Fracture equivalence for ± waves for $\nu = 0.5$

We now show that the elastic interface fields accompanying single ± detachment waves in Sec. III B are strongly reminiscent of moving interface cracks. This wave-fracture analogy is actually exact in the limit $a \to 0$, or, equivalently, $k\Delta x \ll 1$, since it then corresponds to an infinite half space with a single detachment wave. In this case, the analogy is best demonstrated close to either end of the detachment zone for $\nu = 0.5$.

Consider a stationary crack of length l at the interface between two infinite bodies, one of which is rigid and the other elastic with $\nu = 0.5$. For such interface problems, the complex stress intensity factor under combined normal and shear loading is given by [47]

$$K = K_1 + iK_2 = (\sigma_r + i\tau_r)\sqrt{\pi l/2}. \tag{19}$$

It is certainly tempting to directly compare our present problem to one of a static interface crack, especially given the strength of the stress singularity, see Eq. (5). In fact, such a comparison is common for quasistatic JKR-type adhesion problems under shear loading [48,49]. However, we must note two important subtleties in our case. First, our problem is one of elastodynamics in an essentially singular limit. This singular behavior is due to the nature of the remote boundary conditions—while the normal boundary condition (σ_r specified) is the same as with the static crack problem, the tangential condition is not. In fact, specification of a remote velocity V_0, which clearly does not have an equivalent in the static case, prevents us from directly applying this fracture analogy in the tangential direction. The description is valid as $V_0 \to 0^{\pm}$, but breaks down when $V_0 = 0$, for this then corresponds simply to a 1D frictionless normal contact problem. The possibility of propagating waves causing finite interface slip does not arise at all in such a case. Secondly, we have already seen that the normal and tangential dynamics are completely decoupled for $\nu = 0.5$ so that the detachment

wave-fracture analogy can be spelt out in the z direction first. Further, as mentioned above, we can mimic the case of a single crack in an infinite body by setting $a \to 0$ in our formulation.

The interface normal stress may be rewritten from Eq. (5) as

$$\sigma = \frac{\sigma_r |\tan \eta/2| \sec \alpha/2}{\sqrt{\tan^2 \eta/2 - \tan^2 \alpha/2}} \tag{20}$$

and is valid for both $\pm$ waves by accounting for the sign of c/V_0.

As we approach the leading edge of the wave, $\eta = \alpha + \Delta\alpha$, with $\Delta\alpha \to 0^+$, the denominator may be factored using a Taylor series expansion in $\Delta\alpha$ as

$$\begin{aligned}\sigma &= \left.\frac{\sigma_r \tan(\alpha/2) \sec \alpha/2}{\sqrt{2 \tan \alpha/2}\sqrt{\tan(\alpha/2 + \Delta\alpha/2) - \tan \alpha/2}}\right|_{\Delta\alpha \to 0^+} \\ &= \frac{\sigma_r \sqrt{2 \tan \alpha/2}}{\sqrt{k}\sqrt{r}},\end{aligned} \tag{21}$$

where r is the distance (in physical coordinates) from the leading edge of the $\pm$ wave. Given this $1/\sqrt{r}$ dependence, we may define an equivalent mode-I stress intensity factor $K_{\mathrm{I}}^{\mathrm{LE}}$ as

$$K_{\mathrm{I}}^{\mathrm{LE}} = \frac{\sigma_r \sqrt{2\pi \tan \alpha/2}}{\sqrt{k}}, \tag{22}$$

where the superscript LE corresponds to the leading edge of the detachment wave. Since the normal stress is symmetric, the same behavior is also observed at the trailing edge, and we may thus drop the superscript entirely. The expression in Eq. (22) is identical with that for a periodic array of cracks in an infinite solid under normal loading (see, for instance, Ref. [50]).

For $a \ll 1$, $\tan \alpha/2 \sim \alpha/2$ and $\alpha/k = \Delta x/2$ [see Eq. (A3) in Appendix]. The stress intensity factor thus reduces to

$$K_I = \sigma_r \sqrt{\pi \Delta x/2}. \tag{23}$$

Recall that this expression is obtained from the elastodynamic solution after taking $c/c_L, c/c_T \ll 1$ limit, along with $a \ll 1$ above. This is clearly equivalent to the static interface crack solution for $\nu = 0.5$ and one body rigid [45,47]. Hence it is clear that mode I stress intensity factor for a crack of length $2l$ becomes identical with that in Eq. (23) if we replace Δx by $2l$ so that the interface slip, equal to the detachment zone extent, is the equivalent crack size.

The tangential case of mode II shear loading is more illuminating. An equivalent procedure can be repeated as for the normal case, the only change being that we now have to account for which end $\eta = \pm 1$ is the leading edge, depending on which of the $\pm$ waves we are interested in. The interface shear stress is obtained from Eq. (5) as:

$$\tau(\eta) = \left[\tau_r |\tan \eta/2| \pm \frac{2V_0 G}{c}\right] \frac{\sec \alpha/2}{\sqrt{\tan^2 \eta/2 - \tan^2 \alpha/2}}, \tag{24}$$

where $\pm$ depends on which wave is being considered. For the leading edge $+(-)$ is used when $V_0/c > 0 (< 0)$. Taking $\eta = \alpha + \Delta\alpha$ as $\Delta\alpha \to 0^+$, this expression becomes

$$\tau = \left[\tau_r \sqrt{\tan \alpha/2} \pm \frac{2V_0 G}{c\sqrt{\tan \alpha/2}}\right] \frac{1}{\sqrt{kr}} \tag{25}$$

and the corresponding stress intensity factor at the LE of either $\pm$ detachment wave is

$$K_{\mathrm{II}}^{\mathrm{LE}} = \left[\tau_r \sqrt{\tan \alpha/2} \pm \frac{2V_0 G}{c\sqrt{\tan \alpha/2}}\right] \sqrt{\frac{2\pi}{k}} \tag{26}$$

which is dependent on V_0, τ_r, and the wave number k. Clearly this velocity-dependent stress intensity factor is valid for all values of Δx. This "asymmetry" in the mode II stress intensity factor is markedly different from the mode I case and has some important consequences. As mentioned earlier, $V_0 = 0 \Rightarrow \tau_r = 0$ and the limit is singular since it corresponds to a static frictionless problem. One cannot have waves propagating at the interface, each resulting in $\Delta x_\pm$ slip in this situation.

Let us take a closer look at the nondimensional stress intensity factor $\kappa_{\mathrm{II}}^{\mathrm{LE}} = K_{\mathrm{II}}^{\mathrm{LE}} \tau_r^{-1} \Delta x^{-1/2}$ from Eq. (26). Clearly, $\kappa_{\mathrm{II}}^{\mathrm{LE}}$ has two parts with nontrivial dependence on V_0/c. The first part $\sim [\tan(\pi V_0/2c)]^{1/2} (2\pi V_0/c)^{-1/2}$ and the second $\sim (2\pi V_0/c)^{1/2} [\tan(\pi V_0/2c)]^{-1/2}$. For a given boundary value problem with a prespecified V_0, the ratio V_0/c can take any value within the region bounded by $B_\pm$ (solid blue) and the dashed red curves in Fig. 4 with the constraint that $V_0/c < 1$ for all V_0, τ_r. This implies that when $k\Delta x \ll 1$ or $a \ll 1$, the first term approaches a constant, just as with Eq. (23), and as expected for a static fracture problem where $K_{\mathrm{II}} \sim \tau_r \Delta x^{1/2}$.

However when $a \ll 1$, the second term in the expression for $\kappa_{\mathrm{II}}^{\mathrm{LE}}$ does not tend to a constant, but instead $\to G/\tau_r$. In fact, for $a \ll 1$, $\frac{2V_0}{ac} \to \frac{4}{\pi}$ the total expression for the stress intensity factor becomes

$$K_{\mathrm{II}}^{\mathrm{LE}} = (\tau_r + 4G/\pi)\sqrt{\pi \Delta x/2} \qquad \text{when } a \ll 1. \tag{27}$$

In order to use the fracture analogy now, one must make two formal changes to the standard static mode II interface crack problem. In addition to identifying the crack-length $2l$ with Δx as before, we also replace the remote shear τ_r by an " effective shear" $\tau_r + 4G/\pi$.

The extra $4G/\pi$ term is a load-independent contribution to the stress intensity factor and *a priori* appears to be unphysical, since it would then imply the occurrence of stress concentration in the absence of external loading ($\tau_r = 0$). However, looking at its origin in Eq. (26) reveals that it is obtained only in the limit $V_0 \to 0^\pm$ when $\tan \alpha/2 \sim \alpha/2$, but is not valid for $V_0 = 0$. Thus, there are two reasons why interpreting Eq. (27) as a general load-independent stress-intensity factor is misleading. First, it shows that the second term is constant only for very small V_0 but is not present for $V_0 = 0$ exactly. This is, as we've already mentioned, because the case of $V_0 = 0$ is no longer an elastodynamic problem, but instead corresponds to a static problem with no shear. Consequently, there is no mechanism to energetically sustain constant slip-inducing detachment waves. Secondly, in obtaining Eq. (27) from Eq. (26), two factors of V_0 are canceled from the numerator and denominator of the second term, which is clearly not possible when $V_0 = 0$. Retracing its origin to the exact solution, we see that the second term does not arise at all from the governing SIE, Eq. (2) when $V_0 = 0$.

Both mode I and mode II stress concentration factors are functions of the interface slip Δx, nearly equal to the detachment zone width. For $\pm$ waves that effect larger slip, the

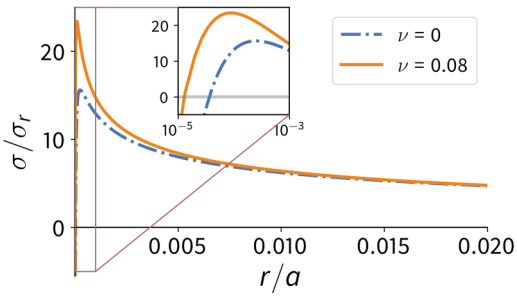

FIG. 9. Normal stress fields showing oscillating singularity near the tip of the detachment zone. Inset is a semilog plot showing the extent of the oscillating zone. It is clear that the maximum stress increases sharply with ν and its location simultaneously approaches the detachment zone tip.

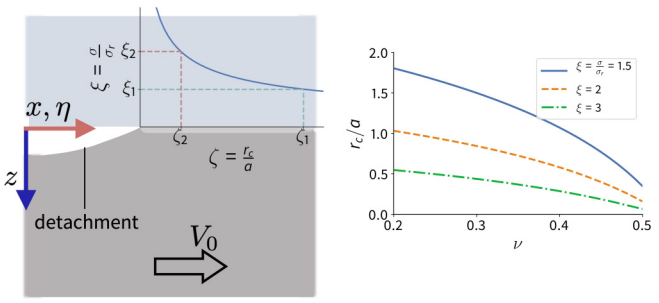

FIG. 10. Stresses ahead of the leading edge of a moving wave. Left: Schematic of the "process zone" ahead of the wave representing the macroscopic effect of microscopic mechanisms that bound the stresses. Right: Process zone size as a function of the Poisson ratio ν, for different cut off values ξ.

stress intensity at the leading edge is larger so that they may propagate at lower remote stress. However, it is important to remember that detachment wave propagation is a fundamentally different process on the macroscale compared to (catastrophic) crack growth. The former results in constant finite tangential slip at the interface, while the latter causes rupture and subsequent interface separation in the normal direction.

E. Fracture equivalence for arbitrary ν: Oscillating singularities and process zones

The fracture equivalence for the general case of $\nu \neq 0.5$ requires a more detailed discussion of the crack-tip stresses. It is well known that for a static crack at a bimaterial interface between one rigid and one elastic body, the stresses show an oscillating singularity. The oscillation region is small, typically about four orders of magnitude smaller than the crack length. The physicality of this oscillating singularity has been the subject of much debate [51,52].

An identical situation appears with detachment waves within our model as well. The equivalent of the Dundurs' parameter β in our case is the ratio $m = \frac{1-2\nu}{2(1-\nu)}$, see Eq. (13). In fact, the final governing SIEs are the same as those for a static crack problem [53], except for additional terms dependent on V_0. Consequently, an oscillatory singularity analogous to the stationary interface crack appears in the stresses, and we use the latter case to illustrate this behavior.

A typical normal stress variation just ahead of the crack-tip is shown in Fig. 9 for $\nu \neq 0.5$. In order to amplify the oscillatory nature of the singularity, we have chosen $\nu = 0, 0.08$. First, for $r/a > 0.01$, the σ/σ_r curves are similar to those obtained earlier (cf. Fig. 7). The crack-tip stresses appear to diverge as $r \to a$ with $\sigma/\sigma_r > 10$. However, as we further approach the crack-tip, say $r \sim 0.02a$, the stresses actually show an oscillating singularity—the apparently diverging stresses show typical $\log(\sin r)$ behavior for $r/a \sim 10^{-4}$, see inset to Fig. 9. This behavior is most pronounced for $\nu = 0$ (dash-dotted blue line) with the maximum stress $\sim 10\sigma_r$ occurring near $r/a \sim 10^{-4}$. As ν increases ($\nu = 0.08$, solid orange curve), the stress peak becomes progressively higher and, simultaneously, its location moves closer to the crack-tip. So much so that for realistic values of $\nu > 0.2$, the peak is very large and occurs at $r/a \sim 10^{-7}$.

The question then naturally arises about whether this type of oscillating singularity has any physical consequences. For this, we argue that, within the framework of linear elasticity, we very well expect that some microscopic mechanism bounds the stresses ahead of the leading edge of a detachment wave. This is analogous to threshold stress or plastic zone models commonly employed in fracture mechanics [54,55]. Let the dimensionless cut-off stress be denoted by $\xi = \sigma/\sigma_r$. For various values of this cut-off threshold, we can evaluate the equivalent process zone size r_c ahead of the leading edge, see Fig. 10. The schematic on the left shows the process zone and stress cut-off for either stress component. The panel on the right of this figure shows the variation of r_c with ν for three different values of ξ.

Three observations may be made from the two graphs in Figs. 9 and 10. In order to estimate a realistic value for ξ, and hence r_c, it is important to consider applied loads that don't violate the validity of the present model. If stresses everywhere within the body are to still obey linear elasticity, say, $|\sigma(x, z)| \leqslant 0.1G$, then $\xi = 10$ would require that $\sigma_r \leqslant 0.01G$. Hence if the threshold value ξ is larger, then the range of permissible (within linear elasticity) remote stresses is smaller. As a result, typical values of $\xi < 5$ provide a realistic estimate of the process zone size for a broader range of remote loads.

It is now clear from Fig. 10 (right) that for these values of ξ, the corresponding cut-off zone size r_c is much larger than the extent of the oscillating zone in Fig. 9. In fact, r_c can never be comparable to the latter since this would require very large $\xi \sim 100$ which is far beyond the domain of validity of the present model. It is also clear from Fig. 10 that r_c decreases for any ν if the threshold ξ is raised. This means that the material can sustain larger opening stresses prior to wave propagation. The precise microscopic mechanisms operating at the leading edge will set the exact value of ξ. Finally, a noticable difference in process zone sizes occurs for $\nu = 0.2$, ranging from $r_c/a \sim 0.5$ to >1.75. Consequently, r_c is sensitive to the chosen threshold ξ and specification of the microscopic mechanisms bounding the stress become important in systems where ν is small.

F. Detachment waves vs. cracks and stick-slip vs. steady sliding

The equivalence between moving detachment waves and interface fracture has important consequences for the onset of sliding at a frictional interface. Given that the transition from static to dynamic friction at an elastic interface is effected by a propagating rupture front resembling a crack [36], one of two sliding modes can occur: stick-slip (via detachment wave propagation) or steady sliding (via rupture or crack growth). Depending on the healing or reattachment mechanism operative at the interface, "mixed" modes could also occur wherein periodic rupture-slip-healing events lead to stick-slip [56]. For the present discussion, we omit this possibility while noting that such ruptures can indeed occur in soft materials like hydrogels, but do not involve significant interface detachment, as with $\pm$ waves [41].

To evaluate which one occurs for a given $\tau_r - \Delta x$ combination, we use the stress intensity factor at the leading edge of the wave, Eq. (23), while making note of its validity for small a. Analogous arguments may be constructed for the more general case. First, for the leading edge of a detachment wave to advance, we require

$$\left(\tau_r + \frac{4G}{\pi}\right)\sqrt{\pi\,\Delta x/2} = \Gamma. \tag{28}$$

In contrast, cracklike propagation at both ends requires

$$\tau_r\sqrt{\pi\,\Delta x/2} = \Gamma. \tag{29}$$

We assume that the fracture toughness Γ is independent of which mode of failure is prevalent—a property quantified by the so-called mode mixity ϑ. Γ usually increases with ϑ but given that $\tau_r \gg \sigma_r$ in the experiments, $\Gamma =$ constant is a reasonable assumption [57]. Secondly, Δx is the equivalent crack length for both possible modes so that the geometry at the leading edge is identical. Finally, the detachment wave solutions we have obtained (Sec. III C) apply over a finite domain and are not just an asymptotic approximation as with static crack fields. So our inferences should apply to both types of $\pm$ waves, at the corresponding leading edge. We also know that the interface cannot sustain detachment waves for far field shear $\tau_r > \tau_r^*$ (see Fig. 4) which forms a boundary in τ-Δx space. Note that for the experiments discussed in Sec. II, $V_0 \sim 10^{-2}$ m/s and the value τ_r^* does not differ significantly from $4G/\pi$. As a final comment, we must emphasize that Eq. (28), being based upon local conditions ahead of the leading edge, is only a necessary condition for d-wave propagation. Sufficiency is ensured by consideration of a suitable readhesion mechanism at the trailing edge of the wave.

Based on these facts, we obtain the phase diagram shown in Fig. 11. The two curves represent Eq. (28) (dash-dotted orange) and Eq. (29) (solid blue) and the horizontal dashed line denotes the limit τ_r^*. The abscissa value at which the orange curve meets the dashed line is denoted Δx_c (vertical dashed line) and plays the role of a critical interface slip. The diagram is applicable to any material pair capable of forming adhesive contact as long as one material is significantly stiffer than the other. The primary geometric requirement is that the dimensions of the contacting solids must be much larger than the crack length.

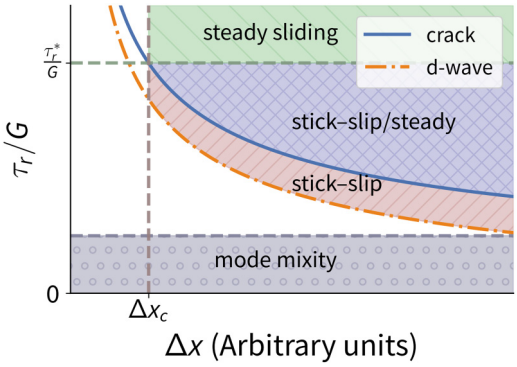

FIG. 11. Phase diagram showing domains of occurrence of $\pm$ detachment waves (d-waves) and, consequently, regions of stick-slip and steady sliding as a function of remote shear stress τ_r/G and interface slip Δx per wave. The solid blue curve represents the stress intensity for shear interface cracks and the dash-dotted orange curve shows the corresponding intensity for detachment wave motion. For $\Delta x < \Delta x_C$ only steady sliding is possible. The limit τ_r^*/G corresponds to limit of validity of the pertubative framework presented.

The diagram must be interpreted as follows. Let us first consider an adhesive interface with an inherent detachment zone of size $\Delta x > \Delta x_c$. As loading at constant remote V_0 is commenced, the interface remains stationary and the resulting remote shear stress increases monotonically from $\tau_r = 0$. When τ_r crosses the dash-dotted orange curve in Fig. 11, the necessary condition for d-wave propagation is satisfied. However, since the interface is stationary, d-wave propagation does not occur immediately and the interface remains stationary with continued increase in τ_r. Once τ_r crosses the solid blue curve, crack propagation begins from the detachment zone. Depending on the strength of readhesion (sufficiency condition for d-wave propagation), we can either have stick-slip or steady sliding beyond this point. If readhesion is strong enough, then the detachment zone begins to translate, with one edge extending and the other closing due to readhesion. Now the τ_r reduces and can fall between the solid blue and dash-dotted orange lines (orange/shaded "//" region) and stick-slip motion ensues. If τ_r remains within the cross-hatched blue region in the figure and if readhesion is not strong enough, then stick-slip does not occur and the initiated crack grows continuously, causing steady interface sliding.

In the complementary case of $\Delta x < \Delta x_c$, increasing τ_r crosses the threshold line τ_r^* prior to satisfying the necessary condition for d-wave propagation. Therefore, only steady sliding is possible in this domain (shaded green "\\"). In the lower region of the phase diagram (shaded gray "○"), where the remote τ_r is small and comparable to (or even smaller than) σ_r, shear and normal direction stresses become coupled so that mode-mixity effects become important. This region of the phase diagram must then be constructed using the numerical solutions computed in Sec. III C.

This entire picture places significant constraints on the nucleation of detachment zones at interfaces. For any material to show stick-slip motion consistently, it must be capable of producing Δx, via either buckling or tensile necking, that is larger than Δx_c. The propensity for producing such a large detachment zone, coupled with ease of wave motion for $\nu \simeq 0.5$,

is likely why polymers readily show stick-slip via detachment wave propagation, while most metals do not.

IV. DISCUSSION

The elastic framework discussed in our work has reproduced the primary observations surrounding the propagation of $\pm$ detachment waves at a soft adhesive interface, viz. the existence of two slow and opposite moving waves, the apparent lack of a definite velocity-scale and the resulting constant interface slip. In addition, the theory and associated numerics also provided expressions for the interface stresses, velocities and displacements. The limit $\alpha \to 0$ is exactly reproduced by the approximate functions used in the numerical scheme. The leading edge of the wave was found to resemble a stationary crack-tip with an effective remote shear stress modified by V_0. This correspondence, along with that between moving cracks and the onset of dynamic friction, allowed the construction of a phase diagram demarcating regions of occurrence of stick-slip and uniform sliding, see Fig. 11. We now discuss some implications of our work as well as potential extensions for future investigation.

A. Comparing theoretical predictions with experimental observations

Having explored the consequences of the theory presented, it is now important to compare the theoretical predictions and explanations presented in Sec. III with the experimental observations in Sec. II. The boundary value problem posed in Eq. (2) depends, in addition to material constants G, ν, on the loading conditions τ_r and V_0, as well as $\Delta x_\pm$. A complete model that accounts for nucleation *outside* the interface will be capable of predicting Δx via suitable considerations of surface buckling or tensile detachment. Consequently, the present model, dealing only with wave propagation, assumes a value for $\Delta x_\pm$ *a priori*. Given this value, any wave number k and α can be chosen within the shaded region bounded by $B_\pm$ in Fig. 4. It is noteworthy that this allows for infinite possible wave speeds, unlike usual wave propagation problems where the speed is fixed by a velocity-scale in the problem. Additionally, the question of which wave will propagate in any given situation is also indeterminate—both $\pm$ waves are equally likely. However, the corresponding tensile or compressive nucleation mechanisms have very different dependence on the applied V_0. It is also possible that, given a sufficiently long channel, both waves are nucleated at either end of the adhesive contact channel (Fig. 1). In most cases, the strong V_0 dependence of these mechanisms means that $+$ waves are more pronounced at higher V_0 compared to $-$ waves. This is in fact borne out by prior experimental observations [38].

Given a choice of $c_\pm$ from within the permissible zone in Fig. 4, the theory quantitatively predicts the corresponding interface displacements, velocities and stresses within the linear elastic approximation and for any arbitrary ν. Several features of this calculation are self-evident with the experiments. For instance, the occurrence of a tensile normal stress at the edges of the sticking zone are very similar to those seen in static adhesive contacts [46] and adhesive sliding experiments using spherical indenters [48]. This is despite the fact that adhesion has not been explicitly included in our model, either in the governing equations or as boundary conditions. It is quite possible that these field predictions, along with possible nonlinear effects, can be quantitatively compared with additional detailed experiments, see for instance Ref. [58]. Stresses can be measured (in the xz plane) using photoelasticity and the corresponding displacements determined either from Hooke's law or directly via digital image correlation methods. We hope to pursue this in the near future.

B. General implications for detachment wave propagation

Some implications of our analytical and numerical results are now discussed. Firstly, the entire framework does not necessitate the use of an interface friction law. Indeed, the boundary value problem introduced in Sec. III applies irrespective of any friction law between the indenter and the sliding elastic body. Second, as shown in Fig. 4, propagation speeds for detachment waves can vary over a range of allowed values. The precise one observed depends on wave nucleation details and the width of the detachment zone. Coupled with the first implication, this means that description of slow moving waves does not need any *a priori* slow velocity scale introduced into the problem via an interface friction law, as is commonly done [59]. It must, however, be mentioned that an additional source for such a velocity scale could well be the material's viscoelastic response. Incorporating this into the present framework is a formidable task and one is forced to take recourse instead to more simplistic formulations [60].

Thirdly, the results for arbitrary $\nu \neq 0.5$ show that the effective " process zone" ahead of a moving wave is sensitive to the microscopic mechanisms at the edge of the detachment zone. This is even more important for metals and crystalline materials in general, where formation of a detachment zone via either tensile necking or compressive buckling is a difficult process. In such cases, the primary recourse to accurately determine the cut-off stress and process zone size is via molecular dynaimcs simulations [61] and physically motivated cohesive zone models [62]. For incompressible materials such as rubbery polymers, this is not so; infinite tensile stresses at the edges of contact are in fact a common feature in linear elastic adhesion problems [46].

C. Analogs of slow detachment waves in other soft sliding systems

Based on our results, two very close analogies may be made for $\pm$ waves. The first is between these waves and elastic dislocations: dislocations also move under a remote shear load and result in plastic slip along the glide plane. This slip is also a signed quantity in the same way that Δx is, being always parallel to V_0. In fact, such an analogy, for Schallamach $(+)$ waves specifically, had been postulated by Gittus in his theory of "interfaceons" at bimaterial interfaces [63]. This work, though clearly unaware of the possibility of $-$ waves at interfaces, provides a simple model to estimate the remote stresses necessary to effect wave motion. Similar dislocation-like models have also been proposed for delamination defects in composite interfaces [64].

The second analogy pertains to the locomotion of soft-bodied invertebrates and has already been alluded to previously [38]. Since these organisms lack any limbs, they must locomote via suitable muscular movements that occur in the form of waves. Specifically, two types of detachment waves have been identified in these organisms [34,65]. Looping locomotion is seen in caterpillars and involves a local buckle that traverses from tail to head when the organism moves forward. Likewise, retrograde waves can result from an extension of the organism's head—a tensile zone— and traverse from head to tail. It is clear that the mechanics of these waves, effected by local muscular elasticity, has much in common with the $\pm$ waves described in this manuscript. However, putting these biological wave motions into a suitable elastic framework will involve analysis of slender objects, which is beyond the scope of the present work. It is hoped that such an analysis will also shed light on possible nucleation mechanisms applicable to the $\pm$ waves described here.

D. Viscoelastic and relaxation effects

Our theoretical description of $\pm$ waves is based on linear elasticity and it is perhaps imperative to discuss the role of viscous relaxation. PDMS is well known to exhibit linear viscoelastic behavior in the small strain or displacement regime [28], a feature that is, in fact, evident in our experiments as well. At low V_0, corresponding to long experimental timescales, viscoelastic relaxation effects are clearly visible for $-$ waves, see Fig. 3 (right). Here, the force trace shows a mean decline over a timescale of $\sim 0.2t_0$, or approximately 1 s, typical of viscoelastic relaxation. These effects, though important, have not been accounted for in the present work. Furthermore, it is at present not clear how one can even begin to incorporate these viscoelastic effects within an analogous half-space model. The primary complication arises from the possibility of multiple Rayleigh-type surface wave solutions [66]. Consequently, constructing an equivalent *ansatz* for the viscoelastic half-space problem is nontrivial, even if the formidable task of solving such an algebraically complex model is notwithstanding. Having said this, there does exist a treatment of generic stick-slip disturbances in viscoelastic media [41]. However this work uses a Coulomb friction model and homogeneous boundary conditions to make the problem amenable to stability analysis. Unfortunately, both these conditions are invalid in the case of $\pm$ detachment waves so that a fundamentally different approach is necessary. The well-known viscoelastic-elasticity analogy offers some hope of making the problem tractable, but the resulting equations are rather unwieldy and require careful consideration. We are presently evaluating some possibilities along these lines and are hopeful that some progress can be made.

E. Limitations of the periodic framework

It is important to outline when the entire framework leading to Eq. (2) is valid and what its limitations are. We recall that our formulation is based on the use of a periodic boundary condition along the propagation direction as well as a co-moving coordinate system. To the best of our knowledge, this type of framework was first proposed by Comninou, Dundurs and coworkers [16,19], see also the discussion by Freund [42]. The framework is itself applicable under the following general conditions. First, the waves being described must necessarily be nondispersive, which, in our work, is borne out by experimental observations, see Fig. 2. Second, periodic boundary conditions imply that we are not solving for a single wave but an infinite array of detachment waves. In the present case, this is again justified by the fact that stick-slip occurs only via propagation of single $\pm$ detachment waves (at any instant) that are generated at a constant frequency, as shown in our earlier work [38]. Finally, the use of periodic boundary conditions takes away the need to specify initial conditions. While this makes the analysis simpler, this simplicity is manifest as an ambivalence towards which wave ($+$ or $-$) is actually propagating at the interface, and is reflected in the symmetric bifurcation diagram (Fig. 4). The downside is that without taking into account the initial conditions (determined by dynamics of the free surface outside the contact zone), one cannot make any prediction about which wave will occur in a given situation nor the extent of resulting slip $\Delta x_{\pm}$.

V. CONCLUSIONS

When an elastic body is slid against a rigid body at constant remote velocity, the contact interface often demonstrates stick-slip motion. Our work has shown an intimate link between this intermittent interface slip and the propagation of detachment waves. Two detachment waves—Schallamach (or $+$ waves) and separation pulses (or $-$ waves) occur, with unique frequency and velocity of propagation. They move parallel ($+$) and antiparallel ($-$) to the applied remote velocity, but cause slip in the same direction. The properties of these waves are directly obtained by using *in situ* imaging techniques.

An elastodynamic framework was presented to describe these waves theoretically. The resulting singular integral equations allowed two distinct wave solution branches, corresponding to $\pm$ waves at the interface. The interface stresses, displacements and velocities were obtained in closed form for incompressible elastic materials and a numerical scheme was used to determine these fields for more general cases. Based on these results, it was found that the leading edge of $\pm$ detachment waves resembles a stationary bimaterial interface crack. Several features of interface fracture also appear in our formulation, including an $r^{-1/2}$ dependence for $\nu = 0.5$ and oscillating singularity ahead of the crack tip for $\nu \neq 0.5$. Based on this analogy, and the correspondence between interface fracture and the onset of steady sliding, a phase diagram was developed to determine when stick-slip via detachment waves would occur vis-á-vis steady sliding.

ACKNOWLEDGMENTS

The authors acknowledge financial support from the Indian Institute of Science Bangalore and partial funding support from the Science and Engineering Research Board (SERB), Government of India, under Grant No. CRG/2018/002058.

APPENDIX: COUPLED SINGULAR INTEGRAL EQUATION FORMULATION

As discussed in the text, we set the detached zone in comoving angular coordinates $\eta = k(x - ct)$ as $-\alpha < \eta < \alpha$, with the rest of the interface ($\alpha < |\eta| < \pi$) in sticking contact. Here, as in the text, k is the wave number and $|\eta| < \pi$ comprises the entire contact. The resulting mixed boundary conditions are

$$\sigma, \tau \begin{cases} = 0 & \eta \in (-\alpha, \alpha) \\ \neq 0 & \alpha < |\eta| < \pi \end{cases} \qquad \dot{u}_x, \dot{u}_z \begin{cases} \neq 0 & \eta \in (-\alpha, \alpha) \\ = 0 & \alpha < |\eta| < \pi \end{cases}. \tag{A1}$$

The stresses σ and τ are normal and tangential to the interface, respectively. The far-field ($z \to -\infty$) stresses are denoted σ_r and τ_r, respectively and the remote sliding speed is V_0. Note that only one of either τ_r or V_0 can be specified, the other is a response; in our case V_0 is applied, as in the experiments described in Sec. II. In addition to this, the following conditions also have to be satisfied. First, once the wave completely passes any point within the interface, it causes that point to slip by a distance Δx. Second, points on the interface must physically always move in the direction of imposed V_0 (signed quantity), irrespective of wave motion direction, cf. Fig. 2. Therefore, we have

$$u_x(\eta) = \begin{cases} 0 & \text{before wave} \\ \Delta x & \text{after wave passage} \end{cases}$$
$$\frac{\dot{u}_x(\eta)}{V_0} \geqslant 0 \quad \forall\, \eta \in (-\pi, \pi). \tag{A2}$$

Note that before (after) wave corresponds to $\eta > \alpha$ ($\eta < -\alpha$) if the wave speed $c > 0$ and the inverse if $c < 0$. Physical conditions of wave propagation, viz. that only a single wave exists within the contact zone and that slip occurs solely due to wave motion, require that the wave parameters α (detachment zone extent) and k (wave number) be related to the experimental parameters V_0, Δx as [38]

$$\alpha = \pi \left| \frac{V_0}{c} \right| \qquad k = \frac{2\pi}{\Delta x} \left| \frac{V_0}{c} \right| \tag{A3}$$

so that the entire problem is posed in terms of the imposed V_0, and experimentally measurable parameters c, Δx.

The description above, along with the partial differential equations (PDEs) of elastodynamics within the domain $z \leqslant 0$ constitute a fully specified boundary value problem in terms of the interface displacements or velocities $\dot{u}_x$ and $\dot{u}_z$. These governing PDEs can be simplified to yield two singular integral equations, as described in Ref. [40]. First, an *ansatz* is used for the displacement fields such that they obey the elastodynamic PDEs. This *ansatz* consists of a superposition of traveling waves that decay exponentially into the bulk and is characterized by two sets of complex constants. Next, the constants are evaluated using the boundary conditions in Eq. (A1) within the detachment zone $|\eta| < \alpha$. This is done using a dual series expansion procedure. Finally, using the fact that the wave speed is much smaller than the longitudinal (c_L) and transverse (c_T) elastic wave speeds, i.e., that $c/c_L, c/c_T \ll 1$ (cf. Sec. II), we perform a perturbation expansion in powers of c/c_L and c/c_T and retain only second-lowest-order terms. The result is a pair of coupled SIEs for the interface velocities $\dot{u}_x$ and $\dot{u}_z$:

$$\begin{aligned} 0 &= \frac{\tau_r}{G} + \frac{2k_1}{\pi}\left[(1 + a^2p^2)\int_{-1}^{1} \frac{\Psi(s)ds}{s - p} + \pi a \frac{V_0}{c} p\right] \\ &\quad - 2k_2(1 + a^2p^2)\Phi(p) \\ 0 &= \frac{\sigma_r}{G} - 2k_2\frac{V_0}{c} + \frac{2k_1}{\pi}(1 + a^2p^2)\int_{-1}^{1} \frac{\Phi(s)ds}{s - p} \\ &\quad + 2k_2(1 + a^2p^2)\Psi(p), \end{aligned} \tag{A4}$$

where the nondimensional functions $\Psi(s)$, $\Phi(s)$ of the interface velocities are as defined in the text [Eq. (1)]. The material constant G is the shear modulus and $a = \tan\alpha/2$. The angular variable η is changed to $p = \frac{\tan\eta/2}{\tan\alpha/2}$ (or s within the integral) and the dimensionless constants $k_1 = \frac{2(1-\nu)}{3-4\nu}$ and $k_2 = \frac{1-2\nu}{3-4\nu}$ where ν is the elastic material's Poisson ratio.

This set of coupled SIEs is the starting point for the analysis in Sec. III [see Eq. (2)] and have to be solved for Φ and Ψ, subject to the additional conditions

$$\int_{-1}^{1} \Psi(s)ds = \frac{\pi V_0}{ac} \qquad \int_{-1}^{1} \Phi(s)ds = 0, \tag{A5}$$

which result from orthogonality of the corresponding Fourier expansions [40]. Note that the SIEs are coupled and of the second-kind, making their solution analytically cumbersome. However, in principle, solving this system for Φ and Ψ gives us the interface velocities directly. From this, the interface normal and shear stresses may be determined as discussed in the text, see the discussion preceding Eq. (5). Interface displacements may be found by directly integrating the velocities $\dot{u}_x$ and $\dot{u}_z$, subject to the conditions in Eq. (A2). This accounts for the occurrence of interface slip due to wave passage.

[1] F. P. Bowden and L. Leben, The nature of sliding and the analysis offriction, in *Proceedings of the Royal Society of London Series A, Mathematical and Physical Sciences* (The Royal Society, London, 1939), pp. 371–391.

[2] E. Rabinowicz, Stick and slip, Sci. Am. **194**, 109 (1956).

[3] W. F. Brace and J. D. Byerlee, Stick-slip as a mechanism for earthquakes, Science **153**, 990 (1966).

[4] F. P. Bowden and D. Tabor, *Friction: An Introduction to Tribology* (Anchor Press/Doubleday, Garden city, New York, 1973).

[5] J. H. Dieterich, Modeling of rock friction: 1. Experimental results and constitutive equations, J. Geophys. Res.: Solid Earth **84**, 2161 (1979).

[6] A. Ruina, Slip instability and state variable friction laws, J. Geophys. Res. **88**, 10359 (1983).

[7] C. H. Scholz, Earthquakes and friction laws, Nature **391**, 37 (1998).

[8] A. Cochard and J. R. Rice, Fault rupture between dissimilar materials: Ill-posedness, regularization, and slip-pulse response, J. Geophys. Res. **105**, 25891 (2000).

[9] K. Ranjith and J. R. Rice, Slip dynamics at an interface between dissimilar materials, J. Mech. Phys. Solids **49**, 341 (2001).

[10] R. Burridge and L. Knopoff, Model and theoretical seismicity, Bull. Seismol. Soc. Am. **57**, 341 (1967).

[11] J. H. Cartwright, E. Hernández-García, and O. Piro, Burridge-Knopoff Models as Elastic Excitable Media, Phys. Rev. Lett. **79**, 527 (1997).

[12] C. Muratov, Traveling wave solutions in the Burridge-Knopoff model, Phys. Rev. E **59**, 3847 (1999).

[13] O. M. Braun and M. Peyrard, Crack in the frictional interface as a solitary wave, Phys. Rev. E **85**, 026111 (2012).

[14] J. D. Achenbach, *Wave Propagation in Elastic Solids* (Elsevier, Amsterdam, 2012).

[15] G. G. Adams, Steady sliding of two elastic half-spaces with friction reduction due to interface stick-slip, J. Appl. Mech. **65**, 470 (1998).

[16] M. Comninou and J. Dundurs, Elastic interface waves and sliding between two solids, J. Appl. Mech. **45**, 325 (1978).

[17] R. Stoneley, Elastic waves at the surface of separation of two solids, in *Proceedings of the Royal Society of London Series A, Containing Papers of a Mathematical and Physical Character* (The Royal Society, London, 1924), pp. 416–428.

[18] J. D. Achenbach and H. I. Epstein, Dynamic interaction of a layer and a half-space, J. Eng. Mech. Div. **93**, 27 (1967).

[19] M. Comninou and J. Dundurs, Elastic interface waves involving separation, J. Appl. Mech. **44**, 222 (1977).

[20] J. K. Trømborg, H. A. Sveinsson, J. Scheibert, K. Thøgersen, D. S. Amundsen, and A. Malthe-Sørenssen, Slow slip and the transition from fast to slow fronts in the rupture of frictional interfaces, Proc. Natl. Acad. Sci. USA **111**, 8764 (2014).

[21] T. Baumberger and C. Caroli, Solid friction from stick–slip down to pinning and aging, Adv. Phys. **55**, 279 (2006).

[22] T. Baumberger, C. Caroli, and O. Ronsin, Self-Healing Slip Pulses Along a Gel/Glass Interface, Phys. Rev. Lett. **88**, 075509 (2002).

[23] T. Yamaguchi, M. Morishita, M. Doi, T. Hori, H. Sakaguchi, and J. P. Ampuero, Gutenberg-Richter's law in sliding friction of gels, J. Geophys. Res.: Solid Earth **116**, B12306 (2011).

[24] A. Schallamach, How does rubber slide?, Wear **17**, 301 (1971).

[25] B. Best, P. Meijers, and A. R. Savkoor, The formation of Schallamach waves, Wear **65**, 385 (1981).

[26] M. Barquins, Friction and wear of rubber-like materials, Wear **160**, 1 (1993).

[27] A. A. Koudine and M. Barquins, Formation of micro-ridges on the surface of Schallamach waves propagating in the contact area between a moving rubber sample and a glass lens, J. Adhes. Sci. Technol. **10**, 951 (1996).

[28] C. J. Rand and A. J. Crosby, Insight into the periodicity of Schallamach waves in soft material friction, Appl. Phys. Lett. **89**, 261907 (2006).

[29] Y. Fukahori, P. Gabriel, and J. J. C. Busfield, How does rubber truly slide between Schallamach waves and stick–slip motion?, Wear **269**, 854 (2010).

[30] K. Viswanathan, A. Mahato, and S. Chandrasekar, Nucleation and propagation of solitary Schallamach waves, Phys. Rev. E **91**, 012408 (2015).

[31] D. Vella, A. Boudaoud, and M. Adda-Bedia, Statics and Inertial Dynamics of a Ruck in a Rug, Phys. Rev. Lett. **103**, 174301 (2009).

[32] J. M. Kolinski, P. Aussillous, and L. Mahadevan, Shape and Motion of a Ruck in a Rug, Phys. Rev. Lett. **103**, 174302 (2009).

[33] J. Gray and H. Lissmann, Studies In animal locomotion: VII. Locomotory reflexes in the earthworm, J. Exp. Biol. **15**, 506 (1938).

[34] E. R. Trueman, *Locomotion of Soft-bodied Animals* (Elsevier, Amsterdam, 1975).

[35] M. Barquins, Sliding friction of rubber and Schallamach waves—A review, Mater. Sci. Eng. **73**, 45 (1985).

[36] S. M. Rubinstein, G. Cohen, and J. Fineberg, Detachment fronts and the onset of dynamic friction, Nature **430**, 1005 (2004).

[37] I. Svetlizky, D. S. Kammer, E. Bayart, G. Cohen, and J. Fineberg, Brittle Fracture Theory Predicts the Equation of Motion of Frictional Rupture Fronts, Phys. Rev. Lett. **118**, 125501 (2017).

[38] K. Viswanathan, N. K. Sundaram, and S. Chandrasekar, Stick-slip at soft adhesive interfaces mediated by slow frictional waves, Soft Matter **12**, 5265 (2016).

[39] See Supplemental Material at http://link.aps.org/supplemental/10.1103/PhysRevE.105.045002 for *in situ* movies showing wave propagation.

[40] K. Viswanathan, N. K. Sundaram, and S. Chandrasekar, Slow wave propagation in soft adhesive interfaces, Soft Matter **12**, 9185 (2016).

[41] C. Caroli, Slip pulses at a sheared frictional viscoelastic/nondeformable interface, Phys. Rev. E **62**, 1729 (2000).

[42] L. B. Freund, Discussion: "Elastic interface waves involving separation" (M. Comninou and J. Dundurs), ASME J. Appl. Mech. **44**, 222 (1977); J. Appl. Mech. **45**, 226 (1978).

[43] J. R. Barber, *Contact Mechanics* (Springer, Berlin, 2018).

[44] F. Erdogan, G. D. Gupta, and T. Cook, Numerical solution of singular integral equations, in *Methods of Analysis and Solutions of Crack Problems*, edited by G. Sih (Springer, Berlin, 1973), pp. 368–425.

[45] J. Rice and G. C. Sih, Plane problems of cracks in dissimilar media, J. Appl. Mech. **32**, 418 (1965).

[46] K. L. Johnson, K. Kendall, and A. D. Roberts, Surface energy and the contact of elastic solids, Proc. R. Soc. Lond. A **324**, 301 (1971).

[47] J. Rice, Elastic fracture mechanics concepts for interfacial cracks, J. Appl. Mech. **55**, 98 (1988).

[48] A. Savkoor and G. Briggs, The effect of tangential force on the contact of elastic solids in adhesion, Proc. R. Soc. Lond. A **356**, 103 (1977).

[49] A. Papangelo and M. Ciavarella, On mixed-mode fracture mechanics models for contact area reduction under shear load in soft materials, J. Mech. Phys. Solids **124**, 159 (2019).

[50] E. E. Gdoutos, C. A. Rodopoulos, and J. R. Yates, *Problems of Fracture Mechanics and Fatigue: A Solution Guide* (Springer Science & Business Media, New York, 2013).

[51] M. Comninou, The interface crack, J. Appl. Mech. **44**, 631 (1977).

[52] M. Comninou, The interface crack in a shear field, J. Appl. Mech. **45**, 287 (1978).

[53] D. Schmueser and M. Comninou, The periodic array of interface cracks and their interaction, Int. J. Solids Struct. **15**, 927 (1979).

[54] B. A. Bilby, A. H. Cottrell, and K. Swinden, The spread of plastic yield from a notch, Proc. R. Soc. Lond. A **272**, 304 (1963).

[55] G. I. Barenblatt, The mathematical theory of equilibrium cracks in brittle fracture, Adv. Appl. Mech. **7**, 55 (1962).

[56] E. Bayart, I. Svetlizky, and J. Fineberg, Rupture dynamics of heterogeneous frictional interfaces, J. Geophys. Res.: Solid Earth **123**, 3828 (2018).

[57] K. Liechti and Y. Chai, Asymmetric shielding in interfacial fracture under in-plane shear, J. Appl. Mech. **59**, 295 (1992).

[58] J. Lengiewicz, M. de Souza, M. A. Lahmar, C. Courbon, D. Dalmas, S. Stupkiewicz *et al.*, Finite deformations govern the anisotropic shear-induced area reduction of soft elastic contacts, J. Mech. Phys. Solids **143**, 104056 (2020).

[59] E. A. Brener, S. Malinin, and V. Marchenko, Fracture and friction: Stick-slip motion, Eur. Phys. J. E **17**, 101 (2005).

[60] B. Persson, A simple model for viscoelastic crack propagation, Eur. Phys. J. E **44**, 1 (2021).

[61] J. Wang, A. Tiwari, B. Persson, and I. Sivebaek, Cylinder–flat-surface contact mechanics during sliding, Phys. Rev. E **102**, 043002 (2020).

[62] N. S. Baban, A. Orozaliev, C. J. Stubbs, and Y. A. Song, Understanding interfacial fracture behavior between microinterlocked soft layers using physics-based cohesive zone modeling, Phys. Rev. E **102**, 012801 (2020).

[63] J. H. Gittus, Interfacial dislocations in frictional sliding and interfacial creep: The theory of interfaceons, Philos. Mag. **31**, 317 (1975).

[64] K. Kendall, Adhesion and composites, Compos. Interfaces **4**, 299 (1996).

[65] E. Orowan, Dislocations and mechanical properties, in *Dislocations in metals*, edited by M. Cohen (The American Institute of Mining and Metallurgical Engineers, New York, 1954), pp. 69–195.

[66] P. K. Currie, M. A. Hayes, and P. M. O'Leary, Viscoelastic Rayleigh waves, Q. Appl. Math. **35**, 35 (1977).